

# Deep Optimal Transport for Domain Adaptation on SPD manifolds

Ce Ju and Cuntai Guan *Fellow, IEEE*

**Abstract**—The domain adaptation (DA) problem on symmetric positive definite (SPD) manifolds has raised interest in the machine learning community because of the growing potential for the SPD-matrix representations across many cross-domain applicable scenarios. However, due to the different underlying space, the previous experience and solution to the DA problem cannot benefit this new scenario directly. This study addresses a specific DA problem: the marginal and conditional distributions differ in the source and target domains on SPD manifolds. We then formalize this problem from an optimal transport perspective and derive an optimal transport framework on SPD manifolds for supervised learning. In addition, we propose a computational scheme under the optimal transport framework, Deep Optimal Transport (DOT), for general computation, using the generalized joint distribution adaptation approach and the existing Riemannian-based network architectures on SPD manifolds. DOT is applied to the real-world scenario and becomes a specific EEG-BCI classifier against the cross-session motor-imagery classification from the calibration phase to the feedback phase. In the experiments, DOT exhibits a marked improvement in the average accuracy in two highly non-stationary cross-session scenarios in the EEG-BCI classification, respectively, indicating the proposed methodology’s validity.

**Index Terms**—Domain adaptation, Riemannian Manifolds, Optimal Transport, Symmetric Positive Definite Manifolds, Motor Imagery Classification

## I. INTRODUCTION

The source data distribution is usually not identical to the target data distribution in a cross-domain problem. It is known as the machine learning community’s domain adaptation (DA) problem and has attracted much attention during the past ten years. [1]–[3] To illustrate, a signal in the online testing set is often not a realization of the same process that generates it for the calibration set, which is a typical DA problem in signal processing.

The critical computational issue of DA is to align the data distributions across source domain  $\mathcal{D}_S$  and target domain  $\mathcal{D}_T$ . Especially for a scenario called unsupervised domain adaptation in which the data label is only available in the source domain, the principal idea of tackling this scenario is to improve the classifier’s performance deployed on the target domain using labeled data of a source domain. Apart from many existing approaches to this scenario [4], the optimal transport (OT) approach has been exploited and paved a new path to align the source and target domains more recently. For instance, Country et al. propose a regularized optimal transportation

Ce Ju and Cuntai Guan are with the S-Lab, Nanyang Technological University, 50 Nanyang Avenue, Singapore (emails: {juce0001,ctguan}@ntu.edu.sg). This work has been submitted to the IEEE for possible publication. Copyright may be transferred without notice, after which this version may no longer be accessible.

model so that the classifier can learn from the labeled source data and deploy it on the target data. [5], [6] We call their framework the OT-DA framework in the following paragraph. The strength of the OT-DA framework includes a more simple evaluation of empirical estimation of the data distribution and a stronger capability to exploit the geometry underlying discrete samples. [5]

Within the OT-DA framework, Yair et al. stand out in addressing a novel scenario of the DA problem occurring on symmetric positive definite (SPD) manifolds and formalizing the problem using the OT theory. [7] The direction is promising because the SPD matrix learning plays an increasing role in many disciplines in science and engineering as a powerful data representation, such as diffusion tensor imaging, computer vision, radar signal processing, and brain-computer interface. [8] For example, a representation of 2D images in the covariance matrix is SPD. It has recently emerged in computer vision because of its compactness, robustness to noise, and flexible scalability in many computer vision tasks. As another example, a representation of electroencephalogram (EEG) signals in spatial covariance matrix (SCM) is also SPD and has been studied in the common spatial pattern method of BCIs for 30 years. [9], [10] However, in the work of Yair et al., they only consider the squared  $\ell_2$  Euclidean distance as a cost function  $c(x, y) = \|x - y\|_2^2$ . They derive the closed-form solution to a well-defined OT problem using Brenier’s polar factorization in the Euclidean space [11]. This motivates us to generalize the OT-DA framework on SPD manifolds equipped with a cost function  $c(x, y) = d_g^2(x, y)$ , where  $d_g(\cdot, \cdot)$  is the Riemannian distance. The comparison between Country’s, Yair’s, and our OT-DA framework is summarized in Table I.

The generalization of an OT-DA framework on SPD manifolds is challenging. On the one hand, it is hard to develop an effective computational scheme to handle the computational issues on SPD manifolds. Fortunately, there have been many explorations of computations schemes for engineering applications on SPD manifolds with one or many classes of Riemannian metrics. In the early feature-engineering age, Xavier et al., who are inspired by manifold-valued images, such as Diffusion Tensor Imaging, have in-depth studies and discussions of different classes of Riemannian metrics on SPD manifolds for various applications and put forward many (statistical) computational schemes for problems on SPD manifolds. [12]–[17] Barachant et al. view SCMs of EEG signals on SPD manifolds and develop many effective EEG-BCI classifiers influenced by Xavier’s schemes, which profoundly affect BCI applications nowadays. [18]–[22] After the deep learning age, Huang et al. propose a series of novel Riemannian-based network architectures, as the computational schemes,

**TABLE I:** Comparison between Approaches for the OT-DA framework.

	Cost function	Transformation	Underlying Space	Scenario
Country et al. [5], [6]	$c(x, y) = \ x - y\ _2^2$	Affine	Euclidean Space	General purpose in domain adaptation
Yair et al. [7]	$c(x, y) = \ x - y\ _2^2$	Bi-map	SPD Manifolds	General purpose in domain adaptation
Ours	$c(x, y) = d_g^2(x, y)$	Bi-map	SPD Manifolds	Drifts in the marginal and conditional distributions

for learning on SPD manifolds with one or many classes of Riemannian metrics. [23]–[25] Utilizing Huang’s network architectures, we develop a geometric deep learning framework called Tensor-CSPNet to exploit the temporospatiotfrequency features behind SCMs on SPD manifolds for the EEG-BCI classification and eventually boost the performance. [26], [27] Hence, the success of Tensor-CSPNet enables Huang’s network architectures to be a perfect computation scheme for dealing with the DA problem on SPD manifolds.

On the other hand, generalizing an OT-DA framework on SPD manifolds might be hard to realize a practical value in real-world applications. To show you what I mean, due to the variability of brain signals, a BCI system is usually not reliable and robust from the calibration phase to the feedback phase. The calibration and feedback phases consist of a cross-session scenario in the EEG-BCI classification in which two sessions are different in distributions. It is a DA problem on SPD manifolds if SCMs of EEG signals are considered to lie on SPD manifolds. There is undoubtedly no label for signals in the feedback phase. Moreover, since SCMs are generated from a set of various frequency bands (e.g., non-overlap and equal band length suggested in [28]) to increase the discrimination between classes, they may not obey any explicit probability distribution (e.g., Gaussian distribution on SPD manifolds). These challenges motivate us to develop a more universal and practical technique for an OT-DA framework on SPD manifolds. Hence, we generalize the classical joint distribution adaptation (JDA) approach [29] on SPD manifolds. This is because the classical JDA approach can handle more practical real-world scenarios in which it jointly adapts both marginal and conditional distributions between domains, even for an implicit probability distribution, at the same time, the label information for the target domain is not required.

This study addresses a challenging real-world scenario in which the source and target domains on an SPD manifold are different in both (implicit) marginal and conditional distributions. The target domain data are not labeled. We formalize such a real-world scenario in the OT-DA framework on SPD manifolds equipped with the Log-Euclidean metric (LEM) [12]. Under the OT-DA framework, we prove a recovery theorem that the hidden relation between the source and target domains can be recovered by putting forward a novel c-concave function on discrete samples of SPD matrices and deriving a closed-form solution to the OT-DA problem on SPD manifolds using the generalized polar factorization on Riemannian manifolds [30]. Finally, we propose a neural network-based computational scheme that we call Deep Optimal Transport (DOT) to exploit the DA problem on SPD manifolds. The computational scheme DOT consists of the existing network architectures on SPD

manifolds, including the BiMap layer, the ReEig layer, and the LOG layer, equipped with a generalized JDA approach on SPD manifolds. Implementing the generalized JDA approach is simple under LEM and trackable on SPD manifolds.

In the experiments, we will pick a critical problem in the robust BCIs called the cross-session motor imagery (MI)-EEG classification as a scenario for evaluating DOT. In the cross-session MI-EEG classification, we calibrate the model on one session and test it on the other. Due to large-scale patterns of synchronized neuronal activity continually changing over time by electrophysiological studies, the brain signals acquired by the EEG device exhibit considerable variability across sessions. Hence, it is challenging that has not been well-addressed.

The remainder of this paper is organized as follows: Section II elaborates on the mathematical background of SPD manifolds equipped with LEM and introduces the JDA approach and neural networks on SPD manifolds. The subsequent section IV establishes the OT-DA framework on Riemannian Manifolds, proposes a computational scheme DOT, and adapts it with three assumptions for the EEG-BCI classification. The performance of Tensor-CSPNet is then compared on a broad set of experiments in Section V, and cautious discussions of several issues are in Section VII. In Appendix, we prove the equivalence between two theorems, the history of the study of nonstationary EEG, the Monge-Kantorovich Formulation, and different Riemannian metrics on SPD manifolds and their properties.

## II. PRELIMINARY

### A. Notations

$Gl(n) := \{ S \in \mathbb{R}^{n \times n} : \det S \neq 0 \}$  is the general linear group.  $\mathcal{S}^n := \{ S \in Gl(n) : S = S^\top \}$  is the space of  $n \times n$  real symmetric matrices, and  $\mathcal{S}_{++}^n := \{ S \in \mathcal{S}^n : x^\top S x > 0, \forall x \in \mathbb{R}^n \setminus \{0\} \}$  is the space of  $n \times n$  real SPD matrices. The *Frobenius* inner product and *Frobenius* norm on  $m \times n$  matrices  $A$  and  $B$  are defined as  $\langle A, B \rangle_{\mathcal{F}} := \text{Tr}(A^\top B)$  and  $\|A\|_{\mathcal{F}}^2 := \langle A, A \rangle_{\mathcal{F}}$  respectively.

### B. Joint Distribution Adaptation

Given a labeled source domain  $\mathcal{D}_S = \{x_s, y_s\}_{s=1}^n$  and an unlabeled target domain  $\mathcal{D}_T = \{x_t\}_{t=1}^m$ , we assume the feature space  $X_S = X_T$  and label space  $Y_S = Y_T$ , whereas the marginal distributions  $P_S(X_S) \neq P_T(X_T)$  and conditional distribution  $Q_S(Y_S|X_S) \neq Q_T(Y_T|X_T)$ . The goal of JDA is to learn a prediction model  $f : x_s \in \mathcal{D}_S \mapsto y_t \in \mathcal{D}_T$  explicitly reducing the distribution differences between both marginal distribution  $P_S(X_S)$  and  $P_T(X_T)$ , and conditional distributions  $Q_S(Y_S|X_S)$  and  $Q_T(Y_T|X_T)$ .

### III. SPD MANIFOLDS WITH THE LOG-EUCLIDEAN METRIC

The space of  $n \times n$  real SPD matrices  $\mathcal{S}_{++}^n$  is given a commutative *Lie* group structure if equipped with a logarithmic multiplication  $\odot$  such that  $S_1 \odot S_2 := \exp(\log(S_1) + \log(S_2))$  for  $S_1, S_2 \in \mathcal{S}_{++}^n$ , where  $\exp$  and  $\log$  are matrix exponential and logarithm respectively. [12, Def. 3] A Log-Euclidean metric is a (Lie-group) bi-invariant metric defined on  $\mathcal{S}_{++}^n$  such that the left- and right-multiplication by any  $S \in \mathcal{S}_{++}^n$  are isometries. The Riemannian manifold  $\mathcal{S}_{++}^n$  with Log-Euclidean metric is denoted as  $(\mathcal{S}_{++}^n, \text{LEM})$  in this paper. The Log-Euclidean distance between any two matrices  $S_1$  and  $S_2$  on  $(\mathcal{S}_{++}^n, \text{LEM})$  is given by

$$d_{\text{LEM}}(S_1, S_2) := \|\log(S_1) - \log(S_2)\|. \quad (1)$$

The Log-Euclidean Fréchet mean  $\text{Bar}_w(\mathcal{B})$  of a batch  $\mathcal{B}$  of SPD matrices  $\{S_i\}_{i=1}^{|\mathcal{B}|} \in (\mathcal{S}_{++}^n, \text{LEM})$  is given in [12, Thm. 6] as follows,

$$\text{Bar}_w(\mathcal{B}) := \exp\left(\frac{1}{|\mathcal{B}|} \cdot \sum_i w_i \cdot \log(S_i)\right). \quad (2)$$

For a more in-depth material for Riemannian geometry of SPD matrices, we refer the readers to [8], [31], [32].

#### A. Network Architectures on SPD manifolds

The network architectures on SPD manifolds include the following layers:

- BiMap: This layer transforms the covariance matrix  $S$  using the bi-map transformation  $W \cdot S \cdot W^T$ . Transformation matrix  $W$  is required to be full row rank.
- ReEig: This layer is analogous to ReLU in classical deep neural networks that introduces the non-linearity on SPD manifolds using  $U \cdot \max(\epsilon I, \Sigma) \cdot U^T$ , where  $S = U \cdot \Sigma \cdot U^T$ , and  $\epsilon$  is a rectification threshold and  $I$  is an identity matrix.
- LOG: This layer is to map elements on SPD manifolds on its tangent space using  $U \cdot \log(\Sigma) \cdot U^T$ , where  $S = U \cdot \Sigma \cdot U^T$ .

They are given in SPDNet [24], which is a deep learning architecture fed with SPD matrices that preserves the SPD matrices across layers during non-linear learning.

### IV. METHODOLOGY

This section will formalize the DA problem on SPD manifolds in the OT framework on Riemannian manifolds, especially SPD manifolds. We call the new framework as the OT-DA framework on SPD manifolds. The OT-DA framework is established on discrete empirical distributions to handle a machine learning problem. Formally, given a measurable space  $X$  and  $Y$ , an empirical distribution of the measure  $\mu \in X$  and  $\nu \in Y$  are written as follows,

$$\mu := \sum_{i \in I} p_i \delta_{x_i}, \text{ and } \nu := \sum_{j \in J} q_j \delta_{y_j},$$

where discrete random variable  $X$  takes values  $\{x_i\}_{i \in I} \in X$ , countable index set  $I$  is with weights  $\sum_{i \in I} p_i = 1$ ;  $Y$  takes values  $\{y_j\}_{j \in J} \in Y$ , countable index set  $J$  is with weights  $\sum_{j \in J} q_j = 1$ ; Dirac measure  $\delta_s$  denotes a unite point mass

at the point  $s \in X$  or  $Y$ . The discrete Monge-Kantorovich problem in the OT theory is given as follows

$$\min_{\gamma \in \prod(\mu, \nu)} \langle \gamma, c(x, y) \rangle_{\mathcal{F}}, \quad (3)$$

where transportation plan  $\gamma \in \prod(\mu, \nu) := \{\gamma \in \mathbb{R}_{\geq 0}^{|X| \times |Y|} \mid \gamma \cdot \mathbb{1}_{|X|} = \mu, \text{ and } \gamma^T \cdot \mathbb{1}_{|Y|} = \nu\}$ , and  $\mathbb{1}_d$  is a  $d$ -dimensional all-one vector. A brief introduction to the Monge-Kantorovich problem refers to Appendix C.

For the OT-DA framework on Riemannian manifolds, we consider  $X$  and  $Y = \mathcal{M}$ , where Riemannian manifolds  $(\mathcal{M}, g)$  is a connected, compact, and  $C^3$  smooth Riemannian manifold without boundary. The OT-DA framework on  $(\mathcal{S}_{++}^n, \text{LEM})$  is attributed to the following geometric property, which will be discussed in Appendix D.

**Proposition 1.**  $(\mathcal{S}_{++}^n, \text{LEM})$  is a Cartan-Hadamard manifold. It is complete, simply connected, and has everywhere non-positive sectional curvature.

#### A. Recovery Correctness

In this section, we will prove a recovery theorem so that we can use a computational scheme to recover the transformation between the source and target domains by solving a specific OT-DA problem on  $(\mathcal{S}_{++}^n, \text{LEM})$ .

**Theorem 1** (Recovery). *Let the source and target measure  $\mu$  and  $\nu \in \mathcal{P}(\mathcal{S}_{++}^n)$  be only accessible through discrete samples on manifold  $\mathcal{S}_{++}^n$ . Given source samples  $\{S_i\}_{i=1}^N \sim \mu$  and weight matrix  $W \in \text{Gl}(n)$ , suppose target samples  $\bar{S}_i := W \cdot S_i \cdot W^T$ , for  $1 \leq i \leq N$ , the weights in both source and target distributions' empirical distributions are  $1/N$ , and  $i = \arg \min_{1 \leq j \leq N} d_{\text{LEM}}(S_i, \bar{S}_j)$ , for  $1 \leq i \leq N$ . Then, transport  $T(S) = W \cdot S \cdot W^T$  is the solution to the OT Problem 3 provided with a cost function  $c(S, \bar{S}) = d_{\text{LEM}}(S - \bar{S})^2$ , where  $d_{\text{LEM}}$  is Riemannian distance with respect to LEM.*

**Remark.** 1). Theorem 1 generalizes [5, Theorem 3.1] on SPD manifolds under the OT-DA framework on  $(\mathcal{S}_{++}^n, \text{LEM})$ . Primarily, we use the bi-map transformation instead of the affine transformation and squared Riemannian distance instead of squared  $\ell_2$  Euclidean distance in the cost function. In Appendix A, we will point out the relationship between two recovery theorems. 2). Condition  $i = \arg \min_{1 \leq j \leq N} d_{\text{LEM}}(S_i, \bar{S}_j)$ , for  $1 \leq i \leq N$  has practical value in real-world scenario, refer to Assumption 2 in Section IV-C. 3).  $W$  is always required in  $\text{Gl}(n)$  so that an SCM is still SPD after the bi-map transformation.

To prove Theorem 1, let's introduce several basic concepts from the nonsmooth analysis. Formally, Let  $(\mathcal{M}, g)$  be a connected, compact, and  $C^3$  smooth Riemannian manifold without boundary. We say a function  $\psi : \mathcal{M} \rightarrow \mathbb{R} \cup \{-\infty\}$  is c-convex if there exists  $\varphi : \mathcal{M} \rightarrow \mathbb{R} \cup \{\pm\infty\}$  such that

$$\psi(x) = \inf_{y \in \mathcal{M}} (c(x, y) + \varphi(y)).$$

The critical step in the proof of Theorem 1 is attributed to the Brenier's polar factorization on Riemannian manifolds [30], given as follows,

**Lemma 2** (Brenier's Polar Factorization [30]). *Let Riemannian manifolds  $(\mathcal{M}, g)$  be a connected, compact, and  $C^3$  smooth Riemannian manifold without boundary. Given any compactly supported measures  $\mu, \nu \in \mathcal{P}(\mathcal{M})$ . If  $\mu$  is absolutely continuous with respect to Riemannian volume, there exists a unique transport map  $T \in S(\mu, \nu)$  as follows,*

$$T(x) = \exp_x(-\nabla\psi(x)),$$

where  $\psi : \mathcal{M} \mapsto \mathbb{R} \cup \{\pm\infty\}$  is a c-concave function with respect to the cost function  $c(x, y) = d_g^2(x, y)/2$ , and  $\exp_x(\cdot)$  is the exponential map at  $x$  on manifolds.

Theorem 1 will be proved by constructing a c-concave function  $\psi(x)$  on  $\mathcal{M}$  and then deriving its corresponding optimal transport map  $T(x)$  using Lemma 2. To begin with, we prove a lemma for the general  $(\mathcal{M}, g)$  as follows,

**Lemma 3.** *On a compact set  $\mathcal{U} \subset \mathcal{M}$  and a fixed  $y \in \mathcal{U}$ , consider the squared distance function  $f(x) = d_g^2(x, y)/2$ . Then, the gradient of  $f$  on  $x \notin \partial\mathcal{M}$  is given as follows,*

$$\nabla f(x) = -\log_x(y).$$

*Proof of Lemma 3.* The proof of Lemma 3 is based on the common arguments in differential geometry. Since  $x \in \mathcal{M}^\circ$ , there exists an open neighbor  $\mathcal{N}$  of  $x$  and  $\epsilon > 0$  such that the exponential map  $\exp_x$  maps the ball  $\mathcal{B}(0, \epsilon) \subset T_x\mathcal{M}$  diffeomorphically onto  $\mathcal{N}$ . [31, Corollary 5.5.2.] Let  $c(s)$  be a geodesic on  $\mathcal{N}$ , parameterized with constant speed, with  $c(0) := y \in \mathcal{N}$  and  $c(1) := x$  with  $\dot{c}(0) = \log_y(x)$ . By reversing the direction of geodesic  $c(1-s)$ , we have  $\dot{c}(1) = -\log_x(y)$ . In the rest part, we will derive that the derivative of  $f$  by linearizing  $\exp_x(v) \in \mathcal{N}$  around  $0 \in T_x\mathcal{M}$  and  $\exp_y(\cdot)$  around  $\dot{c}(0) \in T_y\mathcal{M}$  as follows,

$$\begin{aligned} & f(\exp_x(v)) \\ &= d_g^2(\exp_x(v), y)/2 \\ &= |\log_y(\exp_x(v))|_y^2/2 \\ &= |\dot{c}(0) + (D\log_y)_{\dot{c}(0)}((D\exp_x)_0 v) + o(|v|_x)|_y^2/2 \\ &= |\dot{c}(0)|_y^2/2 + g_y(\dot{c}(0), (D\log_y)_{\dot{c}(0)} v) + o(|v|_x) \\ &= d_g^2(x, y)/2 + g_x(\dot{c}(1), v) + o(|v|_x), \end{aligned}$$

where the differential  $(D\exp_p)_q(\cdot) : T_q(T_p\mathcal{M}) \mapsto (T_p\mathcal{M})$ . The 4-th equality follows from  $(D\exp_x)_0 = I$  on  $T_x\mathcal{M}$ , and the 5-th equality follows from Gauss' lemma [33, Section 3.3.5.]. Hence, by definition of gradient on Riemannian manifolds, we have  $df(x)(v) = g_x(\nabla f(x), v)$ , which implies  $\nabla f(x) = \dot{c}(1) = -\log_x(y)$ .  $\square$

*Proof of Theroem 1.* In the setting of Theorem 1 where the source and target mearue  $\mu, \nu \in \mathcal{P}(\mathcal{S}_{++}^n)$  are only accessible through discrete samples on  $\mathcal{S}_{++}^n$ , source samples  $\{S_i\}_{i=1}^N \sim \mu$  and target samples  $\{\bar{S}_i\}_{i=1}^N \sim \nu$  are given. Let  $\varphi(\bar{S}) := +\infty$  for any  $\bar{S} \in \mathcal{S}_{++}^n$  and  $c(x, y) := d_{LEM}^2(x, y)/2$ . Hence, the corresponding c-concave function is given as follows,

$$\psi(S) = \min_{\{\bar{S}_1, \dots, \bar{S}_N\}} d_{LEM}^2(S, \bar{S})/2.$$

Fix  $S_i$ , we have  $\bar{S}_i = \arg \min_{\{\bar{S}_1, \dots, \bar{S}_N\}} d_{LEM}^2(S_i, \bar{S})/2$ , i.e.,  $\psi(S_i) = d_{LEM}^2(S_i, \bar{S}_i)/2$ . According to Lemma 2 and 3, we derive the optimal transportation map as follows,

$$T(S_i) = \exp_{S_i}(-\nabla\psi(S_i)) = \exp_{S_i}(\log_{S_i}(\bar{S}_i)) = \bar{S}_i.$$

Since  $\bar{S}_i = W \cdot S_i \cdot W^\top$ , the optimal transport  $T(S)$  is given as follows,

$$T(S_i) = W \cdot S_i \cdot W^\top,$$

which implies Theorem 1.  $\square$

**Remark.** 1). The proof of Theorem 1 yields an establishment of the OT-DA framework on  $(\mathcal{S}_{++}^n, \text{LEM})$ .

2). For the case of the multi-source domain adaptation, it is trivial to establish a similar theoretical foundation attributed to the mathematical results of the multi-marginal generalization on Riemannian manifolds [34].

## B. Computational Scheme

In this section, a computational scheme, Deep Optimal Transport (DOT), is proposed for the OT-DA framework on  $(\mathcal{S}_{++}^n, \text{LEM})$  based on the recovery theorem. To capture the distribution drifts between the source and target domains, the classical JDA approach, including marginal distribution adaptation (MDA) and conditional distribution adaptation (CDA), is generalized on  $(\mathcal{S}_{++}^n, \text{LEM})$ . Briefly, the BiMap layer and two losses (i.e., MDA and CDA losses) in DOT consist of a solver to the specific OT-DA problem on  $(\mathcal{S}_{++}^n, \text{LEM})$ . The network architecture of DOT is also illustrated in Fig. 1, and the MDA/CDA losses are illustrated in Fig. 1 (a) and (b), respectively.

1) *Marginal Distribution Adaptation (MDA) on  $(\mathcal{S}_{++}^n, \text{LEM})$ :* The aim of MDA is to adapt marginal distributions  $P_S(X_S)$  and  $P_T(X_T)$  on  $(\mathcal{S}_{++}^n, \text{LEM})$ . We measure the statistical difference between them using the Log-Euclidean distance  $d_{LEM}(\text{Bar}_w(\mathcal{B}_S), \text{Bar}_w(\mathcal{B}_T))$  between Log-Euclidean Fréchet means of each batch of source and target samples  $\mathcal{B}_S$  and  $\mathcal{B}_T$ , respectively, in Equ. 1, i.e.,

$$\mathcal{L}_{MDA} := \|\log(\text{Bar}_w(\mathcal{B}_S)) - \log(\text{Bar}_w(\mathcal{B}_T))\|, \quad (4)$$

2) *Conditional Distribution Adaptation (CDA) on  $(\mathcal{S}_{++}^n, \text{LEM})$ :* The aim of CDA is to adapt condition distributions  $Q_S(y_S|x_S)$  and  $Q_T(y_T|x_T)$  on  $(\mathcal{S}_{++}^n, \text{LEM})$ . We follow the approach in [29] in which the authors take into account class-conditional distribution  $Q(X|Y)$  instead of posterior probability  $Q(Y|X)$  and propose to employ pseudo labels  $\hat{y}$  against the unsupervised setting. To measure the statistical difference between  $Q_S(y_S|x_S)$  and  $Q_T(y_T|x_T)$ , we keep on going to use the Log-Euclidean distance  $d_{LEM}(\text{Bar}_w(\mathcal{B}_{S^l}), \text{Bar}_w(\mathcal{B}_{T^l}))$  between the Log-Euclidean Fréchet means of each batch of source and target samples  $S^l := \{x_S \in S | \hat{y}_S = l\}$  and  $T^l := \{x_T \in T | \hat{y}_T = l\}$ , respectively, within the class  $l \in \{1, \dots, L\}$ , in Equ. 1, i.e.,

$$\mathcal{L}_{CDA} := \|\log(\text{Bar}_w(\mathcal{B}_{S^l})) - \log(\text{Bar}_w(\mathcal{B}_{T^l}))\|, \quad (5)$$

**Remark.** 1). Apart from LEM, there are many alternative Riemannian metrics on  $\mathcal{S}_{++}^n$ , i.e., a more popular class

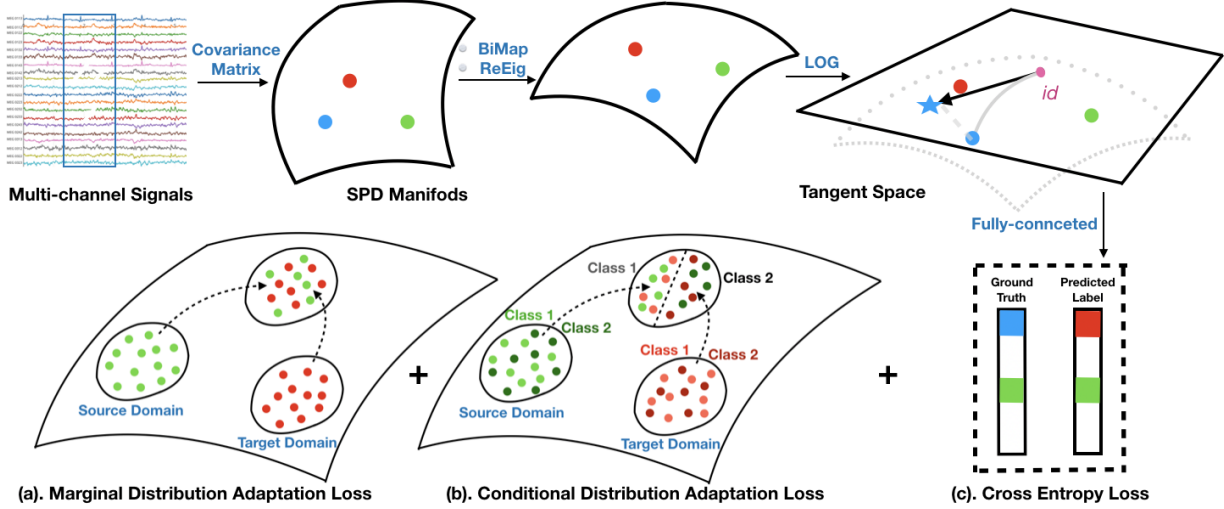


**Fig. 1:** Illustration of the Architecture of Deep Optimal Transport: Data (i.e., multi-channel signals) is first transformed as covariance matrices  $S$  on SPD manifolds using a sliding window, then processed through the BiMap, ReEig, and LOG layers onto the tangent space of SPD manifolds. The loss function takes into account the cross-entropy, MDA loss, and CDA loss on  $(\mathcal{S}_{++}^n, \text{LEM})$ .

of metrics is called the *affine invariant Riemannian metric* (AIRM) [16]. Existing literatures [35] has broadly discussed the learning performance under each metric. However, AIRM is not the best choice in our case because the Fréchet mean on  $(\mathcal{S}_{++}^n, \text{AIRM})$  needs to be calculated in an iteration method as Formula 7, which is not convenient for the neural networks-based approach. Cautious discussions of different Riemannian metrics on SPD manifolds refer to Appendix D.

2). In practice, we plug in Equ. 2 in the generalized MDA (Equ. 4) and CDA (Equ. 5), and let  $w = \{1, \dots, 1\}$ ,  $\mathcal{L}_{\text{LEM}}(\gamma)$ . Then we have two simplified expressions as follows,

$$\begin{aligned}\mathcal{L}_{\text{MDA}} &= \left\| \frac{1}{|\mathcal{B}_S|} \cdot \sum_{S_i \in \mathcal{B}_S} \log(S_i) - \frac{1}{|\mathcal{B}_T|} \cdot \sum_{S_j \in \mathcal{B}_T} \log(S_j) \right\|; \\ \mathcal{L}_{\text{CDA}} &= \left\| \frac{1}{|\mathcal{B}_{S^l}|} \cdot \sum_{S_i^l \in \mathcal{B}_{S^l}} \log(S_i^l) - \frac{1}{|\mathcal{B}_{T^l}|} \cdot \sum_{S_j^l \in \mathcal{B}_{T^l}} \log(S_j^l) \right\|,\end{aligned}$$

which have the following two-fold interpretation with respect to the methodologies in domain adaptation:

On the one hand, they can be viewed as an empirical MMD approach as follows,

$$\text{MMD}(\{S_i\}_{i=1}^n, \{S_j\}_{j=1}^m) = \left\| \frac{1}{n} \sum_{i=1}^n \varphi(S_i) - \frac{1}{m} \sum_{j=1}^m \varphi(S_j) \right\|_{\mathcal{H}}^2,$$

where  $n = |\mathcal{B}_S|$ ,  $m = |\mathcal{B}_T|$ , feature map  $\varphi(x) := \log(x)$ , and reproducing kernel Hilbert space  $\mathcal{H} := \mathbb{R}^d$ , and  $d$  is the output dimension;

On the other hand, since each  $S$  either from  $\mathcal{B}_S$  or  $\mathcal{B}_T$  is the covariance matrix of multichannel signals, it is a correlation alignment (CORAL) approach [36], [37] in which the second-order statistics of the source and target data distributions are aligned to minimize the drift between statistical distributions.

3) Deep Optimal Transport on  $(\mathcal{S}_{++}^n, \text{LEM})$ : Deep transfer learning framework Deep Optimal Transport (DOT) is proposed in this subsection, whose network architecture consists of existing architecture in SPDNet introduced in Section III-A.

The loss function  $\mathcal{L}$  of DOT consists of the cross-entropy (CE) loss  $\mathcal{L}_C$  and the leveraged JDA on  $(\mathcal{S}_{++}^n, \text{LEM})$  including the MDA loss  $\mathcal{L}_{\text{MDA}}$  and the CDA loss  $\mathcal{L}_{\text{CDA}}$ , i.e.,

$$\mathcal{L} := \alpha_1 \cdot \mathcal{L}_C + \alpha_2 \cdot \mathcal{L}_{\text{MDA}}^2 + \alpha_3 \cdot \mathcal{L}_{\text{CDA}}^2, \quad (6)$$

where  $\alpha_1, \alpha_2, \alpha_3 \geq 0$ .

**Remark.** 1). According to Brenier's formulation and McCann's results for optimal transport on Riemannian manifolds [30], the MDA and CDA losses in Equ. 6 are required to be squared distance.

2). According to the multi-marginal optimal transport on Riemannian manifolds [34], the loss function for the multi-source adaptation will be trivially modified as the multi-JDAs between each pair of source and target domains on  $(\mathcal{S}_{++}^n, \text{LEM})$  as follows,

$$\mathcal{L} := \alpha_1 \cdot \mathcal{L}_C + \sum_i \left( \alpha_2^i \cdot \mathcal{L}_{\text{MDA},i} + \alpha_3^i \cdot \mathcal{L}_{\text{CDA},i} \right),$$

where we use subscript  $i$  to represent the  $i$ -th source domain.

3). For an adaptive version of the loss function, one can pre-set the weights  $\alpha_1, \alpha_2$ , and  $\alpha_3$  using adaptive importance weighted tricks with respect to the training and test distributions [38], [39].

4). In the unsupervised domain adaptation, the CDA loss in the JDA approach requires pseudo labels for the test set predicted by a baseline algorithm, and so does our DOT.

5). In the experiments, we use  $\text{DOT}(\alpha_1, \alpha_2, \alpha_3)$  to represent DOT architecture with weights in the loss function  $\alpha_1, \alpha_2$ , and  $\alpha_3$ .

6). The computational scheme DOT is a general machine learning computational scheme applicable to signals and images. We will evaluate it on the EEG-BCI dataset for verification because of its highly non-stationarity across sessions proven in neurophysiology [40]. A brief introduction to the history of the study of nonstationary EEG refers to Appendix B.

### C. DOT as an EEG-BCI Classifier

In the EEG-BCI classification, a multi-channel EEG signals  $X \in \mathbb{R}^{n_c \times n_t}$ , where  $n_c$  and  $n_t$  are number of channels and timestamps. We write SCMs  $S := S(\Delta f \times \Delta t) \in \mathcal{S}_{++}^{n_c}$  to be a EEG signal segment within frequency band  $\Delta f$  and time interval  $\Delta t$ . The illustration of DOT as an EEG-BCI Classifier refers to Fig. 2. The following assumptions are required for the theoretical convergence of the proposed computational scheme in this real-world scenario.

**Assumption 1.** Let  $\mathcal{F}$  and  $\mathcal{T}$  be the frequency and time domains, respectively. Given a segmentation  $\text{Seg}(\mathcal{F}, \mathcal{T}) := \{\Delta f \times \Delta t | \Delta f \subset \text{range}(\mathcal{F}), \text{and } \Delta t \subset \text{range}(\mathcal{T})\}$  on the time-frequency domain of EEG signals. For each segment  $\Delta f \times \Delta t \in \text{Seg}(\mathcal{F}, \mathcal{T})$ , there exists an uniform bi-map weight  $W$  such that the Log-Euclidean Fréchet mean of a batch of source and target samples (1).  $\mathcal{B}_S = \{S_i(\Delta f \times \Delta t)\}_{i=1}$  and  $\mathcal{B}_T = \{\bar{S}_j(\Delta f \times \Delta t)\}_{j=1}$ , respectively, and (2).  $\mathcal{B}_{S^l} = \{S \in \mathcal{B}_S | y = l\}$  and  $\mathcal{B}_{T^l} = \{\bar{S} \in \mathcal{B}_T | y = l\}$ , respectively, under the same label  $l \in \{1, \dots, L\}$ , satisfy the following relationship:

$$\begin{aligned} \text{Bar}(\mathcal{B}_T) &= W \cdot \text{Bar}(\mathcal{B}_S) \cdot W^\top; \\ \text{Bar}(\mathcal{B}_{T^l}) &= W \cdot \text{Bar}(\mathcal{B}_{S^l}) \cdot W^\top. \end{aligned}$$

**Assumption 2.** The average Log-Euclidean distance between the Log-Euclidean Fréchet means of a batch of source and target samples under the same time-frequency segment is the smallest, i.e.,

$$d_{LEM}(\text{Bar}(\mathcal{B}_S), \text{Bar}(\mathcal{B}_T)) \leq d_{LEM}(\text{Bar}(\mathcal{B}_S), \text{Bar}(\mathcal{B}'_T)),$$

where  $\mathcal{B}'_T$  represents a batch of samples generated by  $\Delta f' \times \Delta t \in \text{Seg}(\mathcal{F}, \mathcal{T})$ .

**Assumption 3.** The weights for the Log-Euclidean Fréchet mean of a batch of samples on each segment  $\Delta f \times \Delta t \in \text{Seg}(\mathcal{F}, \mathcal{T})$  in both source and target distributions' empirical distributions are  $1/|\text{Seg}(\mathcal{F}, \mathcal{T})|$ .

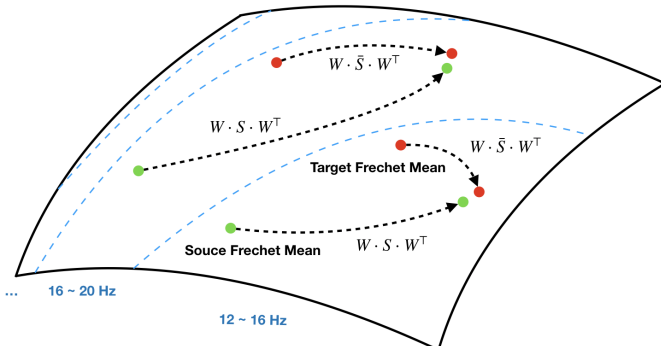


**Fig. 2:** Illustration of DOT as an EEG-BCI Classifier: DOT is an optimal transport on SPD manifolds that parallelly transports the source and target Fréchet means in each frequency band to a common point of the same frequency band. Assumption 1 declares that such a transformation is in a bi-map form with a uniform bi-map weight  $W$ ; Assumption 2 states that each pair of transformations occurs in a frequency band; Assumption 3 guarantees each frequency band equally contributes to the classification.

**Remark.** 1). Assumption 1 requires the uniform bi-map weight  $W$  is independent of representative segment  $\Delta f \times \Delta t \in \text{Seg}(\mathcal{F}, \mathcal{T})$ .

2). Assumption 2 has the practical value: Since the frequency band  $\Delta f$  is usually discretized according to the physiological meaning, i.e.,  $\delta$  (less than 4 Hz),  $\theta$  (4 ~ 7 Hz),  $\alpha$  (8 ~ 13 Hz),  $\beta$  (14 ~ 30 Hz), and  $\gamma$  (above 30 Hz) activity, this assumption prevent the features extracted from different frequency bands to intersect with each other. For our EEG-BCI application, this assumption is justified from a statistical perspective, as discussed in Section VII-D.

3). The technique of Filter Banks: For the EEG-BCI classification, a widely used technique in data processing is the filter bank approach proposed in [28]. The technique of filter banks uses a bank of band-pass filters, i.e., 4 ~ 8 Hz, 8 ~ 12 Hz, ..., and 36 ~ 40 Hz, to decompose the raw oscillatory signals into multiple frequency passbands with the causal Chebyshev Type II filter. This technique enables  $\text{Seg}(\mathcal{F}, \mathcal{T})$  to be a segment set more than one element.

4). Assumption 3 is straightforward because either of the frequency band has an equal priority in the classification.

5). Assumption 1, 2, and 3 together consist of a simplified model for characterizing the domain-invariant representation between sessions of EEG signal.

**Corollary 3.1.** On  $(\mathcal{S}_{++}^{n_c}, \text{LEM})$ , under Assumption 1, 2, and 3, the uniform bi-map weight  $W$  in Assumption 1 is the solution to the OT problem 3 provided with given cost functions 4 and 5.

*Proof.* Theorem 1 yields this corollary directly since Proposition 1 and Assumption 1 ~ 3 consist of all the conditions in Theorem 1.  $\square$

Corollary 3.1 asserts DOT is an optimal transport to adapt the marginal and conditional distributions from the source and target domains on SPD manifolds by parallelly transporting the source and target Fréchet means in each frequency band to a common point of the same frequency band.

## V. EXPERIMENTS

In the experimental part, we will investigate the performance of the proposed computational scheme in two cross-domain scenarios and compare it with other baselines. In addition, we will also visualize the statistical distribution before and after the transformation of RPA and DOT and analyze the transfer performance of the proposed approach.

### A. Evaluation Dataset

In this study, we use the cross-domain MI scenario to evaluate the proposed approach on the largest BCI dataset for 2-class motor imagery, MI-KU [41], as well as the most commonly used benchmarking BCI dataset, BCIC-IV-2a [42].

1) **Korea University Dataset (MI-KU):** In the MI-KU dataset, 54 subjects performed a binary class MI task. Their EEG signals were recorded with a sampling rate of 1,000 Hz and collected with 62 Ag/AgCl electrodes in which 20 electrodes in the motor cortex region were selected (FC-5/3/1/2/4/6, C-5/3/1/z/2/4/5, and CP-5/3/1/z/2/4/6) for our evaluation of each classifier.

2) **BCI Competition IV 2a (BCIC-IV-2a):** BCIC-IV-2a is a cue-based BCI paradigm with the four-class MI-EEG motor imagery task including left hand, right hand, feet, and tongue recorded in 22 Ag/AgCl EEG electrodes and three monopolar EOG channels with 250 Hz sampling rate from 9 subjects. The signal is bandpass-filtered between 0.5 and 100 Hz (with the 50 Hz notch filter enabled). The BCIC-IV-2a dataset has the training session (T) and the evaluation session (E) recorded on different days. In either the T session or E session, each subject performed six runs of 12 cue-based trials for each of the four classes, yielding 288 ( $= 6 \times 12 \times 4$ ) trials per subject.

### B. Experimental Settings

The experimental settings for domain adaptation on two evaluated datasets are stated as follows, illustrated in Fig. 3: 1). Semi-supervised Domain Adaptation: For the MI-KU dataset, Session 1 is for training. The first half of Session 2 is for validation, and the second half is for testing. We adopt early stopping in the validation; 2). Unsupervised Domain Adaptation: For the BCIC-IV-2a dataset, Session 1 is for training, and Session 2 is for testing. There is no validation set in this case, and thus we set a maximum epoch value, for example, 500 for stopping in practice.

**Remark.** We require the knowledge to be always transferred from Session 1 (source domain) to Session 2 (target domain), i.e.,  $S1 \rightarrow S2$  on each dataset. Because there is no neurophysiological meaning if we take the opposite direction in a learning process. Typically, the former and latter sessions correspond to the calibration and feedback phases.

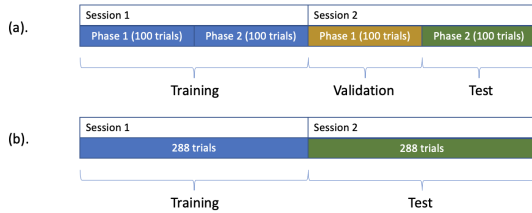


**Fig. 3:** Illustrations for experimental settings of unsupervised domain adaptation on two datasets: (a). MI-KU; (b). BCIC-IV-2a.

### C. Evaluated Baselines

In this section, we select several Riemannian-based baselines in the EEG-BCI classification for evaluation, except FBCSP.

- 1) **FBCSP [28]:** FBCSP employs the CSP method on each sub-bands of EEG signal to acquire sub-band scores and then deploy the machine-learning classifier on selected features. Typically, the performance of BCI classifiers varies widely in data preparation, such as the length of EEG segments and electrode placements. FBCSP's result is regarded as an index for the different experimental settings because of its stable and well-known robust performance.
- 2) **Riemannian-based Classifiers [18]:** The Riemannian-based classifiers refer to two typical classifiers, minimum distance to Riemannian mean (MDM) and tangent space

mapping (TSM), the first two EEG-BCI classifiers to assume SCMs on SPD manifolds. They characterize the geodesic distance on SPD manifolds as a high-level feature for the classification during a feature-engineering process.

- 3) **Riemannian Procrustes Analysis (RPA) [43]:** RPA is a transfer learning-based EEG-BCI classifier using geometric transformations, including translation, scaling, and rotation. After the geometric transformation, RPA uses MDM as the base classifier. Especially, RPA has two subprocesses named Re-center (RCT) process and Rotate (ROT) process. RCT is a process to re-centralize the centroids of data to the identity matrix and equalize the dispersions on each dataset. After RCT, ROT is the process of linking the centroids of each dataset along the geodesics on SPD manifolds.
- 4) **SPDNet [24]:** SPDNet is the first Riemannian-based neural network on SPD manifolds for a general aim. We have introduced it in Section III-A.
- 5) **Tensor-CSPNet [27]:** Tensor-CSPNet is a geometric neural network on SPD manifolds aiming to exploit the temporospatiotfrequency features behind EEG signals for the EEG-BCI classification.

**Remark.** 1). Recently, many attempts have used the techniques from transfer learning to improve a machine learning-based model's performance for the EEG-BCI classification. However, we don't need to compare DOT with these attempts because most of them are not the covariance method. The input of their approach is time series.

2). Riemannian Batch Normalization [44] is not used in DOT. Because it is with AIRM, but DOT is with LEM. We discuss the comparison of both Riemannian metrics in Appendix D.

3). In the original RPA, it has three processes. We combine the first two processes and call it RCT. ROT is a direct numerical approach to solve  $W$  in  $W \cdot S \cdot W^\top = \bar{S}$ . We have a visualized comparison between ROT and DOT in Fig. 4.

## VI. MAIN RESULT

### A. Average Accuracy

In our experiments, FBCSP achieves 59.67% and 65.63% on MI-KU and BCIC-IV-2a, respectively, in Table II. The other covariance methods, TSM and MDM, perform much worse than FBCSP on both datasets. Particularly, since SPDNet doesn't involve the technique of frequency band, it has a significant gap with DOT(1,0,0).

In the unsupervised DA setting, RPA increases by 2.23% and 3.13% upon average accuracies of MDM on two datasets, respectively, attributed to the additional information from the unlabeled test dataset, refer to Table III. It exhibits the baseline effects of the primary transportation of statistical distributions such as re-centering and parallel transport on two datasets. Our proposed DOT approach with the CE loss and either the MDA loss, the CDA loss, or the both always surpasses the one only with the CE loss by 1% ~ 3%. The numerical results show that DOT is as effective as geometric transformations in RPA. However, since the statistical distribution of datasets and the quality of signals affect the increase, it is a dataset-specific result.

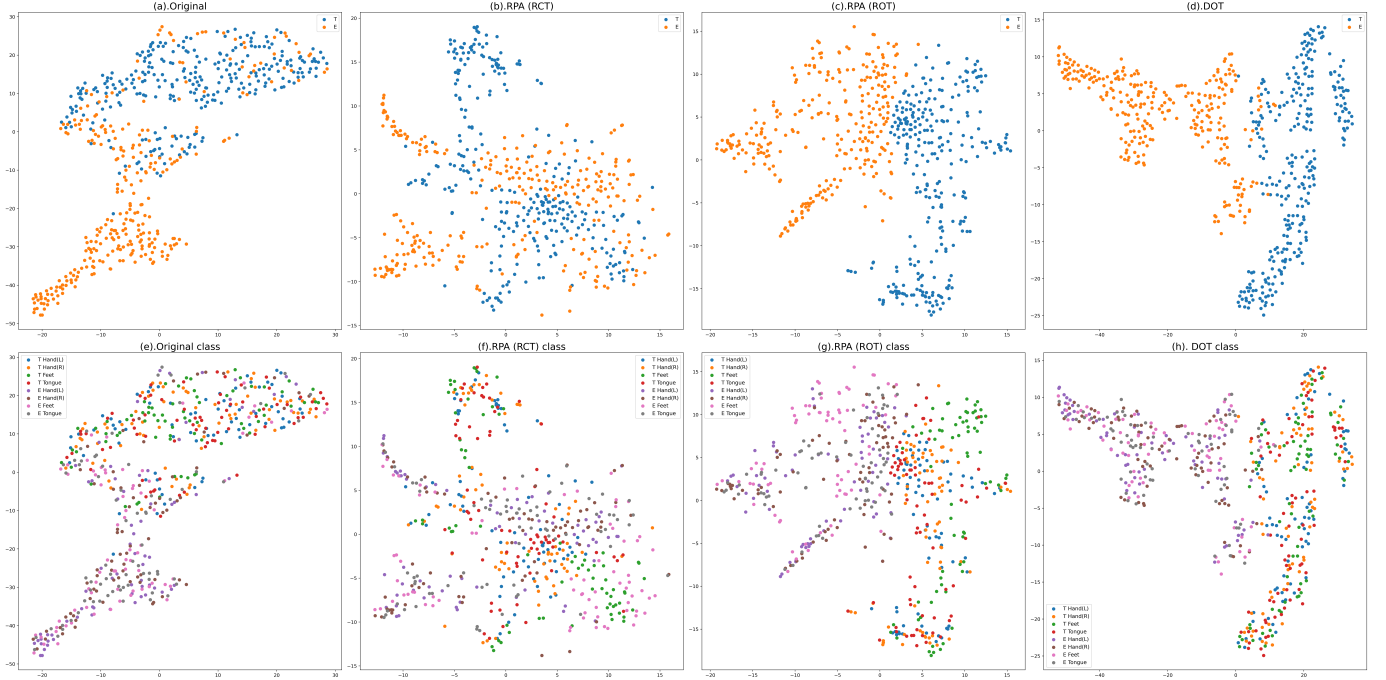


**Fig. 4:** Illustration of comparasions of RPA and DOT on Subject No.5 in the BCIC-IV-2a dataset using t-SNE. We plot the two-dimensional projections of the original signal and the three transformed ones after RCT, ROT, and DOT. Note that ROT is the following step of RCT in RPA. There are 576 points in each subfigure. Half is in the source domain, and the other half is in the target domain. Each point is a two-dimensional dimensionality reduction of the  $9 \times 22 \times 22$ -dimensional tensor. The first line is for their marginal distributions, and the second is for their conditional distributions.

**TABLE II:** Average accuracies in the subject-specific analysis of **MI-KU** (54 Subjects in Total) and **BCIC-IV-2a** (9 Subjects in Total). The best-performing number for each analysis is highlighted in boldface. The triple  $(\alpha_1, \alpha_2, \alpha_3)$  represents the coefficients of the three loss functions of DOT. The methods with \* are the transfer learning approaches training with the labeled training dataset and the unlabeled test dataset.

	MI-KU ( $S_1 \rightarrow S_2$ )	BCIC-IV-2a ( $T \rightarrow E$ )
Method	Acc. (%)	Acc. (%)
FBCSP	59.67	65.63
MDM	52.33	50.69
TSM	51.65	49.65
RPA*	54.56	53.82
SPDNet	60.41	55.56
DOT(1, 0, 0)	63.11	66.24
DOT(1, 1, 0)*	64.24	66.63
DOT(1, 0, 1)*	<b>65.43</b>	65.66
DOT(1, 1, 1)*	64.17	<b>69.17</b>

**Remark.** Although the improvements of algorithms are around 3% in each dataset, they are practical approaches in the domain of BCIs due to a phenomenon of BCI illiteracy, refer to Section VII.

### B. Subject-specific improvements on BCIC-IV-2a

In this section, we print out the subject-specific improvements in BCIC-IV-2a because it is hard to figure out the specific gain caused by DOT just from an average. Table IV shows that aligning the marginal and conditional distributions in the source and target domains benefits the cross-session validation, i.e., Subject No.1, 2, 4, 5, and 6. Aligning the marginal distribution will benefit Subject No.3 and No.9. However, for Subject No.7,

**TABLE III:** Average accuracy increase for the Unsupervised DA setting on **MI-KU** and **BCIC-IV-2a**. The best-performing number for each analysis is highlighted in boldface. Method, A  $\rightarrow$  B, is short for the incremental change from baseline A to novel B.

	MI-KU ( $S_1 \rightarrow S_2$ )	BCIC-IV-2a ( $T \rightarrow E$ )
Transfer Learning Approach	Acc. increase	Acc. increase
MDM $\rightarrow$ RPA	+2.23%	+3.13%
DOT(1, 0, 0) $\rightarrow$ (1, 1, 0)	+1.13%	+0.38%
DOT(1, 0, 0) $\rightarrow$ (1, 0, 1)	<b>+2.32%</b>	-0.58%
DOT(1, 0, 0) $\rightarrow$ (1, 1, 1)	+1.06%	<b>+2.93%</b>

there is no necessity for any aligning. This might be caused by the initial data distribution that we have a brief discussion of it in Section VII-B.

**TABLE IV:** Subject-specific improvements on BCIC-IV-2a. The best-performing number in each row is highlighted in boldface.

Sub	DOT(1, 0, 0)	DOT(1, 1, 0)	DOT(1, 0, 1)	DOT(1, 1, 1)
1	79.86	79.51	72.57	<b>84.03</b>
2	48.61	59.72	51.74	<b>60.76</b>
3	76.04	<b>79.51</b>	77.08	73.96
4	55.90	54.51	53.47	<b>62.15</b>
5	52.43	52.08	56.94	<b>59.72</b>
6	49.65	49.31	52.43	<b>52.78</b>
7	<b>82.99</b>	82.64	77.08	79.86
8	76.39	66.32	<b>78.47</b>	73.61
9	74.31	<b>76.39</b>	71.18	75.69
Avg.	66.24	66.63	65.66	69.17

### C. Visualization

In this section, we plot the dimensionality reduction of transformed data after DOT on the two-dimensional plane using the t-distributed stochastic neighbor embedding (t-SNE) algorithm [45] and analyze the transfer performance of RPA and DOT on the marginal and conditional distributions. Since the cross-entropy (CE) loss in DOT enables it to trade off accuracy and transfer performance, we drop the CE loss in DOT off. In this case, DOT is a pure computational scheme to solve the OT problem on SPD manifolds which aligns the source and target domains together. Subfigures (d) and (h) are the two-dimensional projects of outputs after the bi-map transformation. RPA (RCT & ROT) is a numerical approach to solve  $W$  in  $W \cdot S \cdot W^\top = \bar{S}$ , where  $S$  and  $\bar{S}$  are Riemannian mean of source and target data respectively. The target domain has no label, and thus we compute the rotation for ROT according to its marginal statistics. We notice Subfigure (d) has a similar contour to Subfigure (c). It indicates DOT without the CE loss can take the place of the two processes in RPA and verifies that DOT is a neural network-based approach to solve  $W \cdot S \cdot W^\top = \bar{S}$  from the visualized perspective.

### D. Change of the Log-Euclidean Distance

This subsection plots average Log-Euclidean distances between source and target domains of two datasets. In the construction of the MDA and CDA losses, they are used to measure the Log-Euclidean distances between the marginal and conditional distributions in the source and target domains. In Fig. 5, the curves of the MDA and CDA losses go down steadily towards stability. The final Log-Euclidean distance is usually not zero because the batch size is fixed when the model is learning.

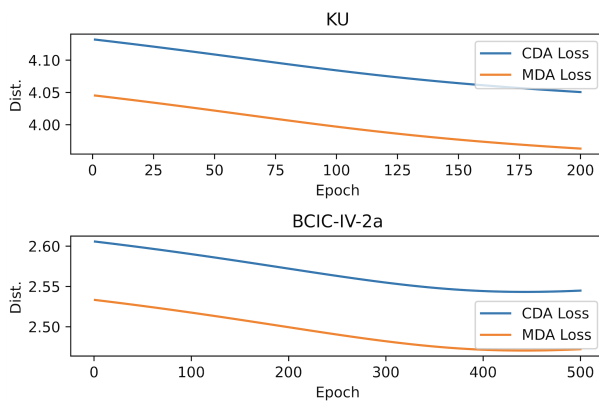


**Fig. 5:** Illustration of average Riemannian distance over epochs on two datasets. Each curve is a sequence of the MDA or CDA loss averages across all the subjects in each dataset during training. The four curves are smooth because we set the size of the whole dataset as the batch size in each iteration.

## VII. DISCUSSIONS

In this section, we will summarize and discuss the ambiguity and limitations of DOT in the following issues.

### A. Integration with Tensor-CSPNet

The proposed computational scheme can be naturally integrated with Tensor-CSPNet. However, two places in the architecture of Tensor-CSPNet need to be modified. On the one hand, to keep the theory self-consistent, Riemannian Batch Normalization with the version of Brooks et al. is not recommended in Tensor-CSPNet because it is with AIRM. On the other hand, the Log-Euclidean Fréchet mean of the batch samples is taken as the average among all SCMs  $\mathcal{S}(\Delta f^* \times \Delta t)$  within the same frequency band  $\Delta f^*$ , for any  $\Delta t \in \text{range}(\mathcal{F})$ . Since there are variants of event-related (de)synchronization (ERD/ERS) occurrence across sessions, we recommend not aligning each SCM in the source domain with one of the same frequency band and time interval in the target domain.

### B. Justification of Distribution Shift

The assumption of marginal and conditional distribution shifts is crucial in our model. However, it varies on subjects and sessions. In this section, we will use t-SNE to visualize the distribution shift on the BCIC-IV-2a dataset and glance at how both marginal and conditional distribution shifts look like and affect the model performance. Fig. 6 illustrates the two-dimensional projection of the training (T) and evaluation (E) sessions of Subject No. 2 and Subject No.5 dimensionally reduced by t-SNE. We notice that both distributions have a noticeable shift, and thus DOT has a marked improvement on these two subjects in Table IV. However, for a subtle shift of the distributions, for example, Subject No.7 and No.8 in Fig. 7, there is not necessary to deploy the DA techniques. Thus, we can see the DOT approach cannot improve the initial result in Table IV.

### C. Rethinking of Assumption 1

The bi-map transformation and the uniformity of the bi-map weights  $W$  are undoubtedly the rough assumptions for a general-purpose framework on SPD manifolds. However, due to the vast complexity of the real-world scenarios, the simplicity of modeling enables the model to work better and be explainable in theory. Luckily, in the proposed computational scheme part, we use the BiMap and ReEig layers, which consist of a nonlinear transformation on SPD manifolds, which might be a remedy for this simplicity.

### D. Justification of Assumption 2

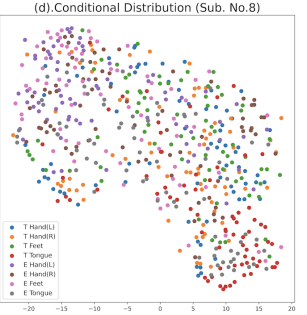
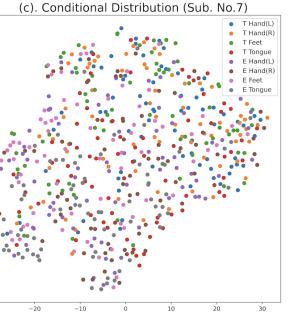
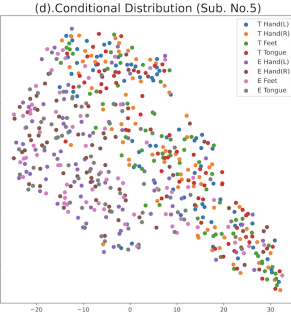
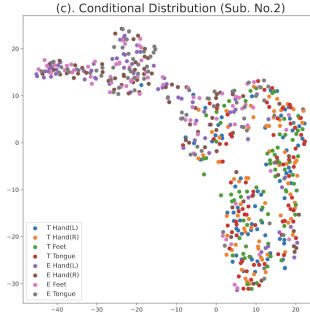
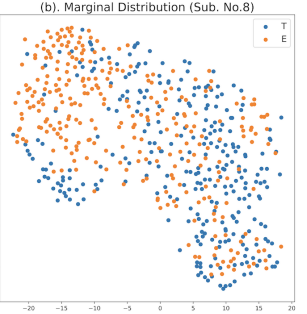
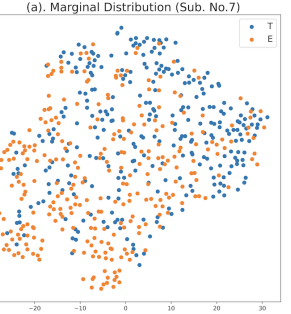
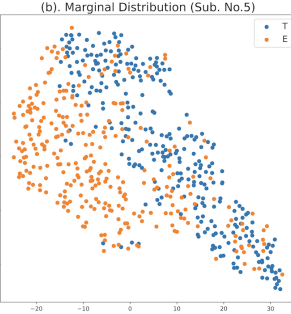
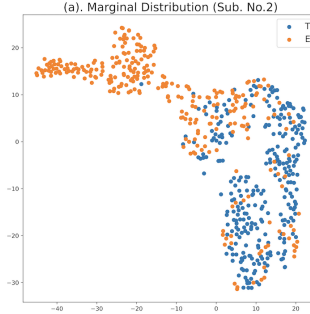
Intuitively, the Log-Euclidean Fréchet means of SCMs generated by the same frequency band in the source and target domains should be the shortest measured by the Log-Euclidean distance, as stated in Assumption 2. The filtered signals within the same frequency band have a closed spectrum. Table V demonstrates that this is a perfect assumption since the diagonal numbers, representing those distances within the same frequency band, are always the smallest of the all row's numbers on both datasets.

**TABLE V:** Average Log-Euclidean distance between the Log-Euclidean Fréchet means of SCMs generated from the different frequency band of the source and target domains on **KU** (54 subjects) and **BCIC-IV-2a** (9 subjects). The shortest distance in each row is highlighted in boldface.

KU: S1 \ S2	4~8 Hz	8~12 Hz	12~16 Hz	16~20 Hz	20~24 Hz	24~28 Hz	28~32 Hz	32~36 Hz	36~40 Hz
4~8 Hz	<b>4.69</b>	4.98	5.82	6.74	7.19	7.64	8.17	8.78	9.28
8~12 Hz	5.09	<b>4.21</b>	4.82	5.81	6.25	6.70	7.22	7.82	8.31
12~16 Hz	5.84	4.76	<b>4.01</b>	4.62	4.98	5.34	5.78	6.30	6.75
16~20 Hz	6.66	5.61	4.37	<b>3.96</b>	4.08	4.33	4.64	5.02	5.40
20~24 Hz	7.08	6.01	4.66	3.97	<b>3.86</b>	3.99	4.27	4.63	4.97
24~28 Hz	7.52	6.45	4.98	4.11	3.86	<b>3.75</b>	3.91	4.21	4.52
28~32 Hz	8.04	6.96	5.40	4.37	4.07	3.82	<b>3.73</b>	3.87	4.11
32~36 Hz	8.65	7.56	5.93	4.77	4.42	4.13	3.88	<b>3.74</b>	3.82
36~40 Hz	9.16	8.07	6.40	5.16	4.77	4.43	4.11	3.82	<b>3.74</b>

BCIC: T \ E	4~8 Hz	8~12 Hz	12~16 Hz	16~20 Hz	20~24 Hz	24~28 Hz	28~32 Hz	32~36 Hz	36~40 Hz
4~8 Hz	<b>2.81</b>	4.25	5.14	5.88	6.70	8.30	9.64	10.97	12.46
8~12 Hz	4.31	<b>2.37</b>	3.98	5.45	6.28	8.07	9.44	10.77	12.26
12~16 Hz	5.16	3.91	<b>2.29</b>	3.53	4.23	5.83	7.15	8.42	9.87
16~20 Hz	5.84	5.49	3.44	<b>2.17</b>	2.76	4.08	5.29	6.56	7.98
20~24 Hz	6.59	6.24	4.18	2.75	<b>2.18</b>	3.31	4.54	5.79	7.24
24~28 Hz	8.11	8.02	5.72	4.01	3.14	<b>2.20</b>	2.96	4.03	5.38
28~32 Hz	9.42	9.38	7.06	5.21	4.39	2.83	<b>2.21</b>	2.86	4.05
32~36 Hz	10.67	10.63	8.25	6.43	5.57	3.87	2.72	<b>2.22</b>	3.05
36~40 Hz	12.16	12.12	9.69	7.85	7.02	5.18	3.85	2.70	<b>2.22</b>



**Fig. 6:** Illustration of the two-dimensional projection of the training (T) and evaluation (E) sessions of Subject No. 2 and Subject No.5 in the BCIC-IV-2a dataset. The upper two subfigures illustrate the shift in the marginal distribution, and the bottom two subfigures demonstrate the conditional distribution shift. The time window of the signal is a 1000-ms length. There is no overlapping between time windows. Each two-dimensional color point is dimensionality reduced from a  $9 \times 20 \times 20$ -dimensional point, where it has 22 electrodes in the motor cortex region and nine frequency bands.

#### E. Dimension of Bi-map Weight $W$

We always require  $W \in GL(n_c)$  because  $W \cdot S \cdot W^\top$  will still lie on  $\mathcal{S}_{++}^{n_c}$ . For the case of  $W \in \mathbb{R}^{d \times n_c}$  ( $d \neq n_c$ ), the bi-map transformation transforms the SPD manifolds with dimension  $n_c^2$  to one with dimension  $d^2$ , and thus it is out of our current framework in which the bi-map transformation is considered. Luckily, it is a trivial extension of Theorem 1 to

**Fig. 7:** Illustration of the two-dimensional projection of the training (T) and evaluation (E) sessions of Subject No. 7 and Subject No.8 in the BCIC-IV-2a dataset. The upper two subfigures illustrate the shift in the marginal distribution, and the bottom two subfigures demonstrate the drift in the conditional distribution. The signal processing is the same as Fig. 6.

the version with any Riemannian map  $f: \mathcal{M} \mapsto \mathcal{M}$ . This is because the proof of Lemma 3 only depends on the endpoint  $y \in \mathcal{M}$  and is independent of the Riemannian map  $f$ .

## VIII. CONCLUSIONS

This study addresses a real-world scenario for domain adaptation on SPD manifolds in which there exist drifts in the marginal and conditional distributions. It proposes a DA-OT framework on SPD manifolds against the real-scenario

DA problem. The theoretical framework yields an effective computational scheme DOT for supervised learning, using the generalized JDA approach and the existing Riemannian-based network architectures on SPD manifolds. We testify the proposed approach on two highly cross-domain BCI scenarios, including semi-supervised and unsupervised scenarios. The numerical results exhibit improvements of 2.32% and 2.93% on the two scenarios' average accuracy, respectively. The visualization results also demonstrate that DOT is a neural network-based solver to the OT problem on SPD manifolds. Hence, we believe the proposed DA-OT framework and the computational scheme DOT yield a novel direction to cope with the DA problem on manifolds.

#### APPENDIX A

THEOREM 1 WITH COST FUNCTION  $c(x, y) = \|x - y\|_2^2$

In this section, we will show Theorem 1 with cost function  $c(x, y) = \|x - y\|_2^2$  is equivalent to [5, Theorem 3.1]. It was first observed and proved by Yair et al.[7] who use the matrix vectorization operator to establish an isometry between the affine transformation and the bi-map transformation. We follow their arguments and revise a bit of their proof.

**Theorem 4.** [5, Theorem 3.1] Let  $\mu$  and  $\nu$  be two discrete distributions on  $\mathbb{R}^d$  with  $N$  Diracs. Given a strictly positive definite matrix  $A$ , bias weight  $b \in \mathbb{R}^d$ , and source samples  $\{x_i^s\}_{i=1}^N \sim \mu$ , suppose target samples  $x_i^t := A \cdot x_i^s + b$ , for  $i = 1, \dots, N$ , and the weights in both source and target distributions, empirical distributions are  $1/N$ . Then, transport  $T(x_i^s) = A \cdot x_i^s + b$  is the solution to the OT Problem provided with a cost function  $c(x^s, x^t) := \|x^s - x^t\|_2^2$ .

To expose the relationship between the bi-map transformation in Theorem 1 and affine transformation in Theorem 4, we introduce the matrix vectorization operator  $\text{vec}(\cdot)$  to stack the column vectors of matrix  $A = (a_1 | a_2 | \dots | a_n)$  below on another as follows,

$$\text{vec}(A) := \begin{pmatrix} a_1 \\ a_2 \\ \vdots \\ a_n \end{pmatrix}$$

Then, we have the following lemma.

**Lemma 5.**  $\text{vec}(W \cdot S \cdot W^\top) = (W \otimes W) \cdot \text{vec}(S)$ , where  $\otimes$  is Kronecker product.

*Proof.* Suppose  $S$  is an  $n \times n$  matrix, and  $W^\top = (w_1^\top | w_2^\top | \dots | w_m^\top)$  is the transpose of  $m \times n$  matrix  $W$  with each column vector  $w_i^\top \in \mathbb{R}^n$  ( $i=1, \dots, m$ ). The  $k$ -th column vector of  $W \cdot S \cdot W^\top$  can be written as  $(W \cdot S \cdot W^\top)_{(:,k)} = W \cdot S \cdot w_k^\top = (w_k^\top \otimes W) \cdot \text{vec}(S)$ . Hence, we achieve the

lemma as follows,

$$\begin{aligned} \text{vec}(W \cdot S \cdot W^\top) &= \begin{pmatrix} (W \cdot S \cdot W^\top)_{(:,1)} \\ \vdots \\ (W \cdot S \cdot W^\top)_{(:,m)} \end{pmatrix} \\ &= \begin{pmatrix} w_1^\top \otimes W \\ \vdots \\ w_m^\top \otimes W \end{pmatrix} \cdot \text{vec}(S) \\ &= (W \otimes W) \cdot \text{vec}(S). \end{aligned}$$

□

**Lemma 6.** Suppose  $W \in \mathbb{R}^{n \times n}$  is positive definite, then  $W \otimes W$  is also positive definite.

*Proof.* This is given by a basic fact that suppose  $\{\lambda_1, \dots, \lambda_n\}$  are the eigenvalues of  $W$ , then the eigenvalues for  $W \otimes W$  is  $\{\lambda_1^2, \dots, \lambda_n^2\}$ . Hence,  $W \otimes W$  is positive definite. □

According to Lemma 5 and 6, the bi-map transformation  $W \cdot S \cdot W^\top$  turns to be affine transformation  $A = W \otimes W$ , and thus Theorem 1. Hence, Theorem 1 equipped with the cost function  $c(\text{vec}(x), \text{vec}(y)) = \|\text{vec}(x) - \text{vec}(y)\|_2^2$  is equivalent to Theorem 4.

**Remark.** Although the matrix vectorization operator is an isometry from an SPD matrix to a vector, it cannot preserve the SPD property in SPD matrices.

#### APPENDIX B HISTORY OF THE STUDY OF NONSTATIONARY EEG

In this section, we introduce the history of the study of the nonstationary EEG signals, which is one of the causes of the cross-domain nature in the EEG-BCI classification. The early studies of EEG signals always assume the stationarity of signals underlying the data processing and analysis. However, the essential characteristics of the nonstationarity of EEG signals are almost eliminated under such an assumption. Hence, a new paradigm for analyzing EEG signals is then based on the new assumption of the essential nonstationarity of underlying signals, which might be caused by switching the inherent metastable states of the neural assemblies during brain functioning. [40], [46], [47] In the BCI scenario, the nonstationarity nature of the brain activities leads to the variability from calibration to feedback. In recent years, there have been many literatures related to this topic in the BCI community. [39], [48]–[56] For instance, Sugiyama et al. exploit their covariate shift adaptation approach to BCI scenarios based on the assumption that the difference between domains is characterized as a change in the feature space and conditional distributions remain unchanged as follows,

$$P_S(X_S) \neq P_T(X_T) \text{ and } Q_S(Y_S | X_S) = Q_T(Y_T | X_T),$$

which improves significantly on several tasks better than the state-of-the-art approaches at that time and exhibits real-world applications in which their model is well-fitting on the nonstationarity changes. [38], [39], [53]

**TABLE VI:** Table for several operators on SPD manifolds under the AIRM and LEM metrics.  $D \log$  and  $D \exp$  are the Fréchet derivatives of the principal matrix logarithm  $\log$  and the matrix exponential map  $\exp$  respectively.

	AIRM	LEM
Inner product: $\langle \mathbf{S}_1, \mathbf{S}_2 \rangle_{\mathbf{P}}$	$\text{Tr}(\mathbf{P}^{-1} \cdot \mathbf{S}_1 \cdot \mathbf{P}^{-1} \cdot \mathbf{S}_2)$	$\langle D \log(\mathbf{P})(\mathbf{S}_1), D \log(\mathbf{P})(\mathbf{S}_2) \rangle_{\mathbf{I}}$
Riemannian Exponential: $\exp_{\mathbf{P}}(\mathbf{S})$	$\mathbf{P}^{\frac{1}{2}} \cdot \exp(\mathbf{P}^{-\frac{1}{2}} \cdot \mathbf{S} \cdot \mathbf{P}^{-\frac{1}{2}}) \cdot \mathbf{P}^{\frac{1}{2}}$	$\exp(\log(\mathbf{P}) + D \log(\mathbf{P})(\mathbf{S}))$
Riemannian Logarithm: $\log_{\mathbf{P}}(\mathbf{S})$	$\mathbf{P}^{\frac{1}{2}} \cdot \log(\mathbf{P}^{-\frac{1}{2}} \cdot \mathbf{S} \cdot \mathbf{P}^{-\frac{1}{2}}) \cdot \mathbf{P}^{\frac{1}{2}}$	$D \exp(\log(\mathbf{P}))(\log(\mathbf{S}) - \log(\mathbf{P}))$
Riemannian Geodesic: $\gamma_t(\mathbf{S}_1, \mathbf{S}_2)$	$\mathbf{S}_1^{\frac{1}{2}} \cdot \exp(t \cdot \log(\mathbf{S}_1^{-\frac{1}{2}} \cdot \mathbf{S}_2 \cdot \mathbf{S}_1^{-\frac{1}{2}})) \cdot \mathbf{S}_1^{\frac{1}{2}}$	$\exp((1-t) \cdot \log(\mathbf{S}_1) + t \cdot \log(\mathbf{S}_2))$
Riemannian Distance: $\mathcal{L}(\mathbf{S}_1, \mathbf{S}_2)$	$\ \log(\mathbf{S}_1^{-\frac{1}{2}} \cdot \mathbf{S}_2 \cdot \mathbf{S}_1^{-\frac{1}{2}})\ $	$\ \log(\mathbf{S}_1) - \log(\mathbf{S}_2)\ $
Weighted Fréchet Mean: $\text{Bar}_w(\mathcal{B})$	No Explicit Formula	$\exp\left(\frac{1}{ \mathcal{B} } \cdot \sum_i w_i \cdot \log(\mathbf{S}_i)\right)$

## APPENDIX C MONGE-KANTOROVICH FORMULATION FOR OPTIMAL TRANSPORTATION

French mathematician Gaspard Monge formalized the OT problem in 1781 to find an optimal volume-preserving map between two distributions measured against a cost function. Formally, on two Polish spaces  $X$  and  $Y$ , given a Borel map  $T : X \mapsto Y$ ,  $T_{\#}$  pushes forward  $\mu \in \mathcal{P}(X)$  through  $T$  to  $T_{\#}\mu \in \mathcal{P}(Y)$ , i.e.,  $T_{\#}\mu(E) := \mu(T^{-1}(E))$ , for any borel  $E \subset Y$ . The OT problem in Monge's formulation looks for a Borel map  $T$  to minimize the transport cost as follows,

$$\min_{T \in S(\mu, \nu)} \int_X c(x, T(x)) d\mu(x),$$

where  $S(\mu, \nu)$  is a set of transports that pushes  $\mu$  forward to  $\nu$ , and cost function  $c : X \times Y \mapsto \mathbb{R}_{\geq 0}$  is a given cost function. The Soviet mathematician Leonid Kantorovich achieved significant advances in this field during World War II (1942) by relaxing the Monge's formulation. The Monge-Kantorovich OT problem is revised as follows,

$$\min_{\gamma \in \Pi(\mu, \nu)} \int_{X \times Y} c(x, y) d\gamma(x, y),$$

where  $\pi^X$  and  $\pi^Y$  are the natural projections from  $X \times Y$  onto  $X$  and  $Y$  respectively, and transportation plan  $\gamma \in \Pi(\mu, \nu) := \{\gamma \in \mathcal{P}(X \times Y) | \pi^X_{\#}\gamma = \mu, \pi^Y_{\#}\gamma = \nu\}$ . For a more thorough background and applications on optimal transportation, we refer to the readers [57], [58].

## APPENDIX D RIEMANNIAN METRICS ON SPD MANIFOLDS

In Section III, we have a brief introduction to the *geodesic* and the Log-Euclidean Fréchet mean on  $(\mathcal{S}_{++}^n, \text{LEM})$ . This section will continue to introduce Riemannian metrics on SPD manifolds. When we talk about a Riemannian manifold, we first need to mention the Riemannian metric. Generally, Riemannian metrics are not unique, and each Riemannian metric defines an associated distance and other geometric quantities on manifolds. Among many metrics on  $\mathcal{S}_{++}^n$ , the most common family of Riemannian metrics are the affine-invariant Riemannian metrics (AIRM), which have been put forward independently from information science in the 1980s and many engineering topics around 2005. [15], [16], [59]–[62] To illustrate, in diffusion tensor imaging, AIRM is proposed to circumvent the difficulty in the calculations in Euclidean space; for example, a tensor

swelling effect [63] that is the determinant of the Euclidean average of SPD matrices can be more significant than one of the original SPD matrices. Formally, the class of AIRM is given by a one-parameter family up to global scaling factors as follows,

$$\langle V, W \rangle_P := \text{Tr}(VP^{-1}WP^{-1}) + \beta \text{Tr}(VP^{-1})\text{Tr}(WP^{-1}),$$

where  $\beta > -1/n$ . All AIRM yield the same Levi-Civita connection, and therefore, they have the same Riemannian  $\exp$  and  $\log$  maps at each point, but the Riemannian distances differ. Meanwhile, the sectional, Ricci, and scalar curvatures on  $(\mathcal{S}_{++}^n, \text{AIRM})$  are non-positive. Hence, endowed with AIRM, the SPD manifold becomes a space everywhere with non-positive sectional curvature without the cut-locus globally diffeomorphic to the Euclidean space, which is called a Cartan-Hadamard manifold [64]. There are many good geometric and statistical properties of SPD manifolds as a Cartan-Hadamard manifold, such as the uniqueness of geodesic joining any two SPD matrices, the existence and uniqueness of the mean of a set of SPD matrices, etc.

However, the algorithms on SPD manifolds equipped with AIRM are running slow due to the complex matrix computations. (see Riemannian matrix exponential and logarithm in Table VI.) To remedy this limitation and overcome the swelling effect simultaneously, another family of Riemannian metrics is the Log-Euclidean metric (LEM) endowed to SPD matrices in this paper. The Log-Euclidean metric also has many excellent properties, including invariance by inversion, logarithmic multiplication, an orthogonal transformation, and scaling. An SPD manifold equipped with LEM is a vector space, and thus it is flat and a Cartan-Hadamard manifold. The most comparative advantage for LEM is to simplify the statistics and analysis on SPD matrices. For instance, Table VI records the several operators on SPD manifolds under the AIRM and LEM metrics. The weighted Fréchet mean under LEM has an explicit formula, but the affine-invariant one does not have. In the literature [16], the affine-invariant one is implicitly defined in a barycentric equation and solved iteratively as follows,

$$\mu_{t+1} \leftarrow \mu_t^{\frac{1}{2}} \cdot \exp\left(\frac{\sum_i w_i \cdot \log \mu_t^{-\frac{1}{2}} S_i \mu_t^{-\frac{1}{2}}}{|\mathcal{B}|}\right) \cdot \mu_t^{\frac{1}{2}}. \quad (7)$$

The implicit formula is improper to be used in a loss function, and hence, we use LEM to be the Riemannian metric in this paper. For more details on Riemannian metrics on SPD manifolds, an excellent survey of SPD manifolds is dedicated to [8], [14], [17].

## ACKNOWLEDGMENT

This study is supported under the RIE2020 Industry Alignment Fund–Industry Collaboration Projects (IAF-ICP) Funding Initiative, as well as cash and in-kind contributions from the industry partner(s). This study is also supported by the RIE2020 AME Programmatic Fund, Singapore (No. A20G8b0102).

## REFERENCES

- [1] S. Ben-David, J. Blitzer, K. Crammer, F. Pereira *et al.*, “Analysis of representations for domain adaptation,” *Advances in neural information processing systems*, vol. 19, p. 137, 2007.
- [2] S. J. Pan and Q. Yang, “A survey on transfer learning,” *IEEE Transactions on knowledge and data engineering*, vol. 22, no. 10, pp. 1345–1359, 2009.
- [3] M. Wang and W. Deng, “Deep visual domain adaptation: A survey,” *Neurocomputing*, vol. 312, pp. 135–153, 2018.
- [4] G. Wilson and D. J. Cook, “A survey of unsupervised deep domain adaptation,” *ACM Transactions on Intelligent Systems and Technology (TIST)*, vol. 11, no. 5, pp. 1–46, 2020.
- [5] N. Courty, R. Flamary, D. Tuia, and A. Rakotomamonjy, “Optimal transport for domain adaptation,” *IEEE transactions on pattern analysis and machine intelligence*, vol. 39, no. 9, pp. 1853–1865, 2016.
- [6] N. Courty, R. Flamary, A. Habrard, and A. Rakotomamonjy, “Joint distribution optimal transportation for domain adaptation,” in *Proceedings of the 31st International Conference on Neural Information Processing Systems*, ser. NIPS’17. Red Hook, NY, USA: Curran Associates Inc., 2017, p. 3733–3742.
- [7] O. Yair, F. Dietrich, R. Talmon, and I. G. Kevrekidis, “Domain adaptation with optimal transport on the manifold of spd matrices,” *arXiv preprint arXiv:1906.00616*, 2019.
- [8] H. Q. Minh and V. Murino, “Covariances in computer vision and machine learning,” *Synthesis Lectures on Computer Vision*, vol. 7, no. 4, pp. 1–170, 2017.
- [9] Z. J. Koles, M. S. Lazar, and S. Z. Zhou, “Spatial patterns underlying population differences in the background eeg,” *Brain topography*, vol. 2, no. 4, pp. 275–284, 1990.
- [10] J. Müller-Gerking, G. Pfurtscheller, and H. Flyvbjerg, “Designing optimal spatial filters for single-trial eeg classification in a movement task,” *Clinical neurophysiology*, vol. 110, no. 5, pp. 787–798, 1999.
- [11] Y. Brenier, “Polar factorization and monotone rearrangement of vector-valued functions,” *Communications on pure and applied mathematics*, vol. 44, no. 4, pp. 375–417, 1991.
- [12] V. Arsigny, P. Fillard, X. Pennec, and N. Ayache, “Fast and simple computations on tensors with log-euclidean metrics.” Ph.D. dissertation, INRIA, 2005.
- [13] X. Pennec, “Statistical computing on manifolds for computational anatomy.” Ph.D. dissertation, Université Nice Sophia Antipolis, 2006.
- [14] V. Arsigny, P. Fillard, X. Pennec, and N. Ayache, “Log-euclidean metrics for fast and simple calculus on diffusion tensors,” *Magnetic Resonance in Medicine: An Official Journal of the International Society for Magnetic Resonance in Medicine*, vol. 56, no. 2, pp. 411–421, 2006.
- [15] X. Pennec, “Statistical computing on manifolds: from riemannian geometry to computational anatomy,” in *LIX Fall Colloquium on Emerging Trends in Visual Computing*. Springer, 2008, pp. 347–386.
- [16] X. Pennec, P. Fillard, and N. Ayache, “A riemannian framework for tensor computing,” *International Journal of computer vision*, vol. 66, no. 1, pp. 41–66, 2006.
- [17] X. Pennec, “Manifold-valued image processing with spd matrices,” in *Riemannian geometric statistics in medical image analysis*. Elsevier, 2020, pp. 75–134.
- [18] A. Barachant, S. Bonnet, M. Congedo, and C. Jutten, “Multiclass brain–computer interface classification by riemannian geometry,” *IEEE Transactions on Biomedical Engineering*, vol. 59, no. 4, pp. 920–928, 2011.
- [19] ———, “Classification of covariance matrices using a riemannian-based kernel for bci applications,” *Neurocomputing*, vol. 112, pp. 172–178, 2013.
- [20] M. Congedo, A. Barachant, and R. Bhatia, “Riemannian geometry for eeg-based brain–computer interfaces: a primer and a review,” *Brain-Computer Interfaces*, vol. 4, no. 3, pp. 155–174, 2017.
- [21] R. J. Kobler, J.-I. Hirayama, L. Hehenberger, C. Lopes-Dias, G. R. Müller-Putz, and M. Kawanabe, “On the interpretation of linear riemannian tangent space model parameters in m/eeg,” in *2021 43rd Annual International Conference of the IEEE Engineering in Medicine & Biology Society (EMBC)*. IEEE, 2021, pp. 5909–5913.
- [22] R. J. Kobler, J.-i. Hirayama, and M. Kawanabe, “Controlling the fréchet variance improves batch normalization on the symmetric positive definite manifold,” in *ICASSP 2022-2022 IEEE International Conference on Acoustics, Speech and Signal Processing (ICASSP)*. IEEE, 2022, pp. 3863–3867.
- [23] Z. Huang, R. Wang, S. Shan, X. Li, and X. Chen, “Log-euclidean metric learning on symmetric positive definite manifold with application to image set classification,” in *International conference on machine learning*. PMLR, 2015, pp. 720–729.
- [24] Z. Huang and L. Van Gool, “A riemannian network for spd matrix learning,” in *Thirty-First AAAI Conference on Artificial Intelligence*, 2017.
- [25] Z. Huang, C. Wan, T. Probst, and L. Van Gool, “Deep learning on lie groups for skeleton-based action recognition,” in *Proceedings of the IEEE conference on computer vision and pattern recognition*, 2017, pp. 6099–6108.
- [26] C. Ju, D. Gao, R. Mane, B. Tan, Y. Liu, and C. Guan, “Federated transfer learning for eeg signal classification,” in *2020 42nd Annual International Conference of the IEEE Engineering in Medicine & Biology Society (EMBC)*. IEEE, 2020, pp. 3040–3045.
- [27] C. Ju and C. Guan, “Tensor-cspnet: A novel geometric deep learning framework for motor imagery classification,” *IEEE Transactions on Neural Networks and Learning Systems*, 2022.
- [28] K. K. Ang, Z. Y. Chin, H. Zhang, and C. Guan, “Filter bank common spatial pattern (fbcsp) in brain–computer interface,” in *2008 IEEE international joint conference on neural networks (IEEE world congress on computational intelligence)*. IEEE, 2008, pp. 2390–2397.
- [29] M. Long, J. Wang, G. Ding, J. Sun, and P. S. Yu, “Transfer feature learning with joint distribution adaptation,” in *Proceedings of the IEEE international conference on computer vision*, 2013, pp. 2200–2207.
- [30] R. J. McCann, “Polar factorization of maps on riemannian manifolds,” *Geometric & Functional Analysis GAFA*, vol. 11, no. 3, pp. 589–608, 2001.
- [31] P. Petersen, S. Axler, and K. Ribet, *Riemannian geometry*. Springer, 2006, vol. 171.
- [32] R. Bhatia, *Positive definite matrices*. Princeton university press, 2009.
- [33] M. P. Do Carmo and J. Flaherty Francis, *Riemannian geometry*. Springer, 1992, vol. 6.
- [34] Y.-H. Kim and B. Pass, “Multi-marginal optimal transport on riemannian manifolds,” *American Journal of Mathematics*, vol. 137, no. 4, pp. 1045–1060, 2015.
- [35] K.-X. Chen, J.-Y. Ren, X.-J. Wu, and J. Kittler, “Covariance descriptors on a gaussian manifold and their application to image set classification,” *Pattern Recognition*, vol. 107, p. 107463, 2020.
- [36] B. Sun and K. Saenko, “Deep coral: Correlation alignment for deep domain adaptation,” in *European conference on computer vision*. Springer, 2016, pp. 443–450.
- [37] B. Sun, J. Feng, and K. Saenko, “Correlation alignment for unsupervised domain adaptation,” in *Domain Adaptation in Computer Vision Applications*. Springer, 2017, pp. 153–171.
- [38] H. Shimodaira, “Improving predictive inference under covariate shift by weighting the log-likelihood function,” *Journal of statistical planning and inference*, vol. 90, no. 2, pp. 227–244, 2000.
- [39] M. Sugiyama, M. Krauledat, and K.-R. Müller, “Covariate shift adaptation by importance weighted cross validation,” *Journal of Machine Learning Research*, vol. 8, no. 5, 2007.
- [40] A. Y. Kaplan, A. A. Fingelkurt, A. A. Fingelkurt, S. V. Borisov, and B. S. Darkhovsky, “Nonstationary nature of the brain activity as revealed by eeg/meg: methodological, practical and conceptual challenges,” *Signal processing*, vol. 85, no. 11, pp. 2190–2212, 2005.
- [41] M.-H. Lee, O.-Y. Kwon, Y.-J. Kim, H.-K. Kim, Y.-E. Lee, J. Williamson, S. Fazli, and S.-W. Lee, “Eeg dataset and openbmi toolbox for three bci paradigms: an investigation into bci illiteracy,” *GigaScience*, vol. 8, no. 5, p. giz002, 2019.
- [42] C. Brunner, R. Leeb, G. Müller-Putz, A. Schlägl, and G. Pfurtscheller, “Bci competition 2008–graz data set a,” *Institute for Knowledge Discovery (Laboratory of Brain-Computer Interfaces), Graz University of Technology*, vol. 16, pp. 1–6, 2008.
- [43] P. L. C. Rodrigues, C. Jutten, and M. Congedo, “Riemannian procrustes analysis: transfer learning for brain–computer interfaces,” *IEEE Transactions on Biomedical Engineering*, vol. 66, no. 8, pp. 2390–2401, 2018.

- [44] D. Brooks, O. Schwander, F. Barbaresco, J.-Y. Schneider, and M. Cord, “Riemannian batch normalization for spd neural networks,” *Advances in Neural Information Processing Systems*, vol. 32, pp. 15 489–15 500, 2019.
- [45] L. Van der Maaten and G. Hinton, “Visualizing data using t-sne.” *Journal of machine learning research*, vol. 9, no. 11, 2008.
- [46] A. I. Kaplan, “The nonstability of the eeg: a methodological and experimental analysis,” *Uspekhi fiziolicheskikh nauk*, vol. 29, no. 3, pp. 35–55, 1998.
- [47] A. A. Fingelkurts and A. A. Fingelkurts, “Making complexity simpler: multivariability and metastability in the brain,” *International Journal of Neuroscience*, vol. 114, no. 7, pp. 843–862, 2004.
- [48] C. Vidaurre, A. Schlogl, R. Cabeza, R. Scherer, and G. Pfurtscheller, “Study of on-line adaptive discriminant analysis for eeg-based brain computer interfaces,” *IEEE transactions on biomedical engineering*, vol. 54, no. 3, pp. 550–556, 2007.
- [49] J. d. R. Millán, A. Buttfield, C. Vidaurre, R. Cabeza, A. Schlögl, G. Pfurtscheller, P. Shenoy, and R. P. Rao, “18 adaptation in brain-computer interfaces,” *Toward Brain-Computer Interfacing*, p. 303, 2007.
- [50] B. Blankertz, M. Kawanabe, R. Tomioka, F. U. Hohlfeld, V. V. Nikulin, and K.-R. Müller, “Invariant common spatial patterns: Alleviating nonstationarities in brain-computer interfacing.” in *NIPS*. Citeseer, 2007, pp. 113–120.
- [51] P. Von Bünau, F. C. Meinecke, F. C. Király, and K.-R. Müller, “Finding stationary subspaces in multivariate time series,” *Physical review letters*, vol. 103, no. 21, p. 214101, 2009.
- [52] J. Blumberg, J. Rickert, S. Waldert, A. Schulze-Bonhage, A. Aertsen, and C. Mehring, “Adaptive classification for brain computer interfaces,” in *2007 29th Annual International Conference of the IEEE Engineering in Medicine and Biology Society*. IEEE, 2007, pp. 2536–2539.
- [53] C. Vidaurre, M. Kawanabe, P. von Bünau, B. Blankertz, and K.-R. Müller, “Toward unsupervised adaptation of lda for brain–computer interfaces,” *IEEE Transactions on Biomedical Engineering*, vol. 58, no. 3, pp. 587–597, 2010.
- [54] P. Shenoy, M. Krauledat, B. Blankertz, R. P. Rao, and K.-R. Müller, “Towards adaptive classification for bci,” *Journal of neural engineering*, vol. 3, no. 1, p. R13, 2006.
- [55] Y. Li and C. Guan, “An extended em algorithm for joint feature extraction and classification in brain-computer interfaces,” *Neural computation*, vol. 18, no. 11, pp. 2730–2761, 2006.
- [56] B. A. S. Hasan and J. Q. Gan, “Unsupervised adaptive gmm for bci,” in *2009 4th International IEEE/EMBS Conference on Neural Engineering*. IEEE, 2009, pp. 295–298.
- [57] C. Villani, *Optimal transport: old and new*. Springer, 2009, vol. 338.
- [58] S. Kolouri, S. R. Park, M. Thorpe, D. Slepcev, and G. K. Rohde, “Optimal mass transport: Signal processing and machine-learning applications,” *IEEE signal processing magazine*, vol. 34, no. 4, pp. 43–59, 2017.
- [59] J. Burbea and C. R. Rao, “Entropy differential metric, distance and divergence measures in probability spaces: A unified approach,” *Journal of Multivariate Analysis*, vol. 12, no. 4, pp. 575–596, 1982.
- [60] L. T. Skovgaard, “A riemannian geometry of the multivariate normal model,” *Scandinavian journal of statistics*, pp. 211–223, 1984.
- [61] M. Moakher, “A differential geometric approach to the geometric mean of symmetric positive-definite matrices,” *SIAM Journal on Matrix Analysis and Applications*, vol. 26, no. 3, pp. 735–747, 2005.
- [62] P. T. Fletcher and S. Joshi, “Riemannian geometry for the statistical analysis of diffusion tensor data,” *Signal Processing*, vol. 87, no. 2, pp. 250–262, 2007.
- [63] D. Tschumperle and R. Deriche, “Diffusion tensor regularization with constraints preservation,” in *Proceedings of the 2001 IEEE Computer Society Conference on Computer Vision and Pattern Recognition. CVPR 2001*, vol. 1. IEEE, 2001, pp. I–I.
- [64] P. Li, *Geometric analysis*. Cambridge University Press, 2012, vol. 134.